European Journal of Nuclear Medicine and Molecular Imaging
https://doi.org/10.1007/s00259-026-07769-7

ORIGINAL ARTICLE

# Automated long axial field of view PET image processing and kinetic modelling with the TurBO toolbox

**Jouni Tuisku[1,2] · Santeri Palonen[1,2] · Henri Kärpijoki[1,2] · Aino Latva-Rasku[1,2,3] · Nelli Tuomola[1,2,3] · Harri Harju[1,2] · Sergey V. Nesterov[1,2] · Vesa Oikonen[1,2] · Hidehiro Iida[1,2] · Jarmo Teuho[1,2] · Chunlei Han[1,2] · Tomi Karjalainen[1,2] · Anna K. Kirjavainen[1,5] · Johan Rajader[1,4] · Riku Klén[1,2] · Pirjo Nuutila[1,2,3] · Juhani Knuuti[1,2] · Lauri Nummenmaa[1,2,6]**

Received: 26 October 2025 / Accepted: 6 January 2026


## Abstract

**Purpose** Long axial field of view (LAFOV) PET imaging requires extensive automation due to the large number of target tissues. Therefore, we introduce an open-source analysis pipeline (TurBO, Turku total-BOdy) for automated preprocessing and kinetic modelling of LAFOV [$^{15}$O]$H_2O$ and [$^{18}$F]FDG PET data. TurBO enables efficient, reproducible quantification of tissue perfusion and metabolism at regional- and voxel-levels through automated co-registration, motion correction, CT-based region of interest (ROI) segmentation, image-derived input function (IDIF) extraction, and region-specific kinetic modelling.

**Methods** The pipeline was validated with Biograph Vision Quadra (Siemens Healthineers) LAFOV PET/CT data from 21 subjects scanned with [$^{15}$O]$H_2O$ and 16 subjects scanned with [$^{18}$F]FDG. Six CT-segmented ROIs (cortical brain gray matter, left iliopsoas muscle, right kidney cortex and medulla, pancreas, spleen and liver) were used to assess different levels of tissue perfusion and glucose metabolism.

**Results** Model fits showed high quality with consistent estimates at regional and voxel-levels ($R^2>0.83$ for [$^{15}$O]$H_2O$, $R^2>0.99$ for [$^{18}$F]FDG). Manual and automated IDIFs were in concordance ($R^2>0.74$ for [$^{15}$O]$H_2O$, and $R^2>0.78$ for [$^{18}$F]FDG) with minimal bias (<4% and<10%, respectively). Manual and CT-segmented ROIs showed strong agreement ($R^2>0.82$ for [$^{15}$O]$H_2O$ and $R^2>0.83$ for [$^{18}$F]FDG). Motion correction had little impact on estimates ($R^2>0.71$ for [$^{15}$O]$H_2O$ and $R^2>0.78$ for [$^{18}$F]FDG) compared with uncorrected data.

**Conclusion** The TurBO pipeline provides fully automated and reliable quantification for LAFOV PET data. It substantially reduces manual workload and enables standardized, reproducible assessment of inter-organ perfusion and metabolism.

**Keywords** [$^{15}$O]$H_2O$ · [$^{18}$F]FDG · LAFOV PET · Automated processing · Kinetic modelling · Pipeline

## Introduction

Long axial field of view (LAFOV) PET systems present unique opportunities for scientific research and clinical diagnostics by enabling the simultaneous, non-invasive imaging of multiple organs and their physiological interactions. These systems provide clear benefits, including improved count sensitivity, extended image coverage, and extraction of image-derived input function from the aorta [1]. However, they also introduce new challenges for data analysis. Patient movement is a major concern in LAFOV studies, as complete patient restraining is not possible similarly to e.g., in brain-only studies. In addition, manual pre-processing of LAFOV PET data is time-consuming, especially when analysing multiple tissues. One LAFOV

Jouni Tuisku and Santeri Palonen contributed equally to this work.

✉ Jouni Tuisku
joupes@utu.fi

1 Turku PET Centre, University of Turku, Turku, Finland

2 Turku PET Centre, Turku University Hospital, Po Box 52, 20521 Turku, Finland

3 Department of Endocrinology, Turku University Hospital, Turku, Finland

4 Turku PET Centre, Accelerator Laboratory, Åbo Akademi University, Turku, Finland

5 Turku PET Centre, Radiopharmaceutical Chemistry Laboratory, University of Turku, Turku, Finland

6 Department of Psychology, University of Turku, Turku, Finland

Published online: 31 January 2026

study may contain tens of different regions of interest (ROI), whose delineation alone can exceed a full workday per subject. Furthermore, the manual approach is prone to operator bias, which may reduce reproducibility compared to automated methods [2]. Finally, the complex preprocessing, modelling and data analysis flow warrants comprehensive quality control to ensure accurate outputs at all stages and again, completing all these steps by human operators is simply not feasible.

Any all-inclusive LAFOV PET processing pipeline should handle preprocessing, ROI delineation, and kinetic modelling using various approaches tailored to different radiotracers, which makes the development of a comprehensive PET pipeline a challenging task. While various tools exist for automated brain PET data analysis [2–5], equivalent pipelines for LAFOV PET data are not yet widely available. To address these issues, we introduce an open-source Turku Total-Body PET modelling pipeline (TurBO), which enables automated and reproducible processing and kinetic modelling of LAFOV PET data. It supports various radiotracers and kinetic models, allowing fully automated processing, including co-registration, motion correction, input function determination, and ROI delineation. The pipeline enables both regional and voxel-level kinetic modelling, with the flexibility to apply tissue-specific models, and provides visual and numerical tools for quality control of the preprocessing steps.

Here, we describe and validate the TurBO pipeline (freely available at https://turbo.utu.fi) using [$^{15}$O]$H_2O$ and [$^{18}$F]FDG PET data to benchmark preprocessing and modelling of tissue perfusion and glucose metabolism. We compared the automated image-derived input function (IDIF) with the manually delineated input, assessed results with and without motion correction, evaluated the results of ROI-based and voxel-level kinetic modelling, and compared outcome measures from manually and automatically determined ROIs from data collected with the Biograph Vision Quadra (Siemens Healthineers) 106 cm FOV PET/CT scanner. We hypothesized that TurBO provides a rapid, accurate and reproducible approach for modelling LAFOV PET perfusion and metabolism data at voxel and regional levels.

## Materials and methods

### Overview of TurBO pipeline

TurBO (Turku total-BOdy) pipeline runs on MATLAB (The MathWorks, Inc., Natick, MA, USA) and utilizes openly available tools for data processing (dependencies listed at https://turbo.utu.fi). For all PET kinetic modelling, we use MATLAB implementations of openly available and previously validated in-house software (http://www.turkupetcentre.net/petanalysis).The general framework involves CT to PET registration, PET motion correction, segmentation of the CT image into tissues and organs, automatic image-based input function (IDIF) extraction and finally, kinetic modelling at regional and voxel-levels. The pipeline outputs LAFOV parametric images, separate parametric brain images normalized to MNI space, regional outcome measures as well as quality control metrics. An overview of the workflow is shown in Fig. 1, and the process is described in detail below.

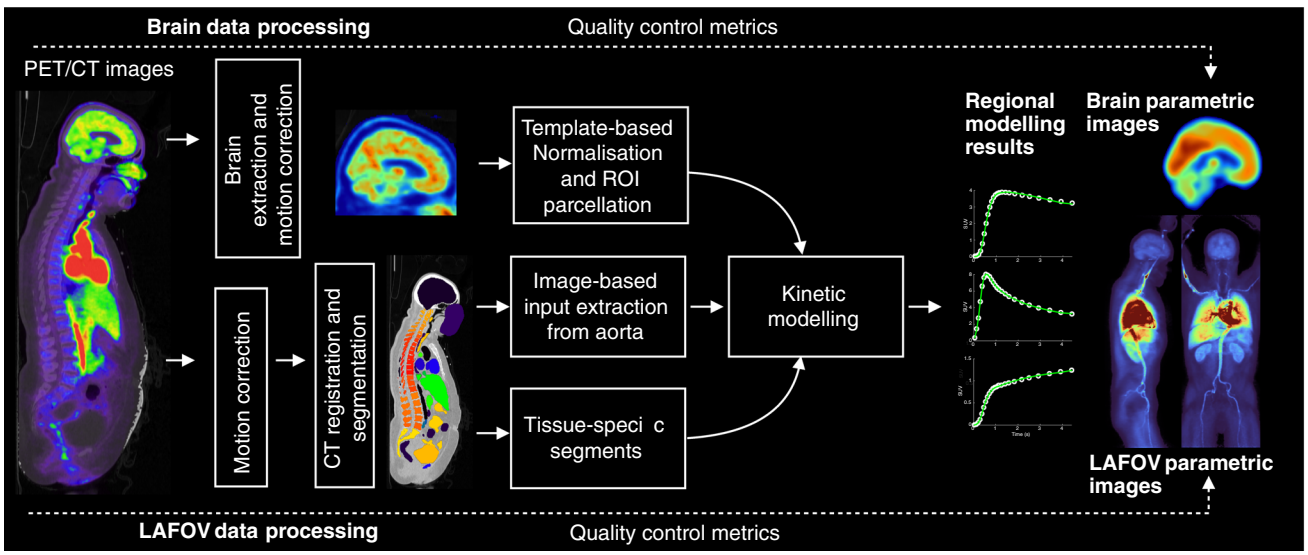


**Fig. 1** Flowchart for the TurBO pipeline

### LAFOV PET data preprocessing and kinetic modelling

DICOM images are first converted to NIfTI using the *dcm2niix* tool [6], and the required metadata such as framing, injected dose, and subject weight is extracted from the DICOM header. Next, PET motion correction is applied following the previously described approach [7], employing a diffeomorphic *greedy* registration algorithm (https://greedy.readthedocs.io). For [$^{18}$F]FDG, the motion correction start frame is determined by normalized cross-correlation (NCC), as described in [7]. In our [$^{18}$F]FDG validation data this varies between 4-6 min. Due to the variation in [$^{15}$O]$H_2O$ distribution, early frames are discarded, and the start frame is selected as the time point where the heart time-activity curve (TAC) falls below half of its peak value (this varies between 15–45 s in our validation data). For both radioligands, the motion correction reference frame is selected as the one with the highest NCC relative to the CT. In our [$^{15}$O]$H_2O$ validation data, this frame is typically near the scan midpoint and in [$^{18}$F]FDG data near the scan endpoint. Subsequently, CT is registered with the PET mean image using the *greedy* algorithm to correct any misalignments and ensuring that CT-based regions of interest (ROIs) correspond with the PET data. The CT image is first resampled to PET voxel size, whereafter the *TotalSegmentator* tool [8] is used for CT-based segmentation of major organs and tissues, to serve as ROIs for PET quantification. Additionally, the segmented ROIs can be trimmed by removing a specified distance from their edges to reduce signal contamination from nearby high-intensity areas, or due to motion. For instance, it may be necessary to exclude spill-in from the cardiovascular system in the segmented liver.

### LAFOV [$^{15}$O]$H_2O$ and [$^{18}$F]FDG PET data modelling

For [$^{15}$O]$H_2O$, a one-tissue compartmental model (1TCM) [9] is fitted for each measured regional time activity curve. The model is defined using the following equations (see **Online Resource**. for details):

$$C_{\mathrm{T}}(T) = K_1 \int_0^T C_{\mathrm{A}}(t) - k_2 \int_0^T C_{\mathrm{T}}(t)$$

$$C_{\mathrm{PET}}(t) = C_{\mathrm{T}}(t) + V_{\mathrm{A}} C_{\mathrm{A}}(t)$$

where $C_{PET}$ is the measured PET activity concentration, $C_T$ is the tissue activity concentration, $C_A$ is the arterial activity concentration corrected for radiotracer delay in tissue, $V_A$ is the arterial volume fraction, $K_1 = f$ describes the blood flow, and $k_2 = f/p$, where $p = K_1/k_2$ is the partition coefficient of water (i.e., distribution volume).

Because the standard 1TCM model fitting with a descending aorta IDIF is not feasible for the liver, the arterial and portal vein blood flow fractions $r_A = f_A/(f_A + f_{PV})$ and $r_{PV} = f_{PV}/(f_A + f_{PV})$, where $f_A$ and $f_{PV}$ represent arterial and portal vein blood flow [10], are first estimated using the dual-input model [11] with the descending aorta IDIF $C_{IDIF}$ and a portal vein input curve $C_{PV}$ (that is estimated using $C_{IDIF}$). Consequently, the resulting combined input

$$C_{\mathrm{liverIF}}(t) = r_{\mathrm{A}} C_{\mathrm{IDIF}}(t) + r_{\mathrm{PV}} C_{\mathrm{PV}}(t)$$

is used for estimating liver parameters with the standard 1TCM (see **Online Resource** for details).

Voxel-level [$^{15}$O]$H_2O$ quantification is carried out using non-negative least squares (NNLS) [12] either by estimating all three 1TCM model parameters ($K_1$, $k_2$, $V_A$), or with basis function approach [13], where discrete $k_2$ values are used for calculating the basis functions, and $K_1$, $V_A$ are estimated with NNLS (see **Online Resource** for details). For both voxel-level methods, the radiotracer delay parameter is estimated separately for each voxel using a lookup-table approach, in which the delay is chosen as the value that yields the best model fit, except in the liver with combined input, where the input and the delay are obtained from the ROI-level quantification.

To quantify glucose metabolism using [$^{18}$F]FDG, the descending aorta IDIF is first converted to plasma [14] using the individual hematocrit measurement, after which regional and voxel-level Patlak plot [15], fractional uptake ratio (FUR) [16] and standardised uptake value (SUV) estimates can be calculated similarly in all regions. Because lumped constant (LC) values that are used in conversion from [$^{18}$F]FDG to glucose uptake are still unknown for most tissue types, we used published LC values only for specific organs [17] ($LC_{brain} = 0.65$, $LC_{myocardium} = 1$, $LC_{muscles} = 1.16$), and $LC = 1$ for all other tissues.

### Image-derived input extraction

For automatic IDIF determination, a separate smaller PET image containing the heart and aorta is extracted from the original LAFOV PET image and corrected for motion using the rigid motion correction method [18], which enables motion correction also for the initial frames. Briefly, the method uses a subject-specific synthetic dynamic reference, generated for each frame from the CT segmentation and the corresponding ROI TACs. Each PET frame is then rigidly co-registered to its matching synthetic reference frame. Consequently, IDIF is extracted from the descending aorta using an automated method based on our centre's standard protocol for manual input delineation: the lower third of the myocardium is used as a higher anatomical landmark to

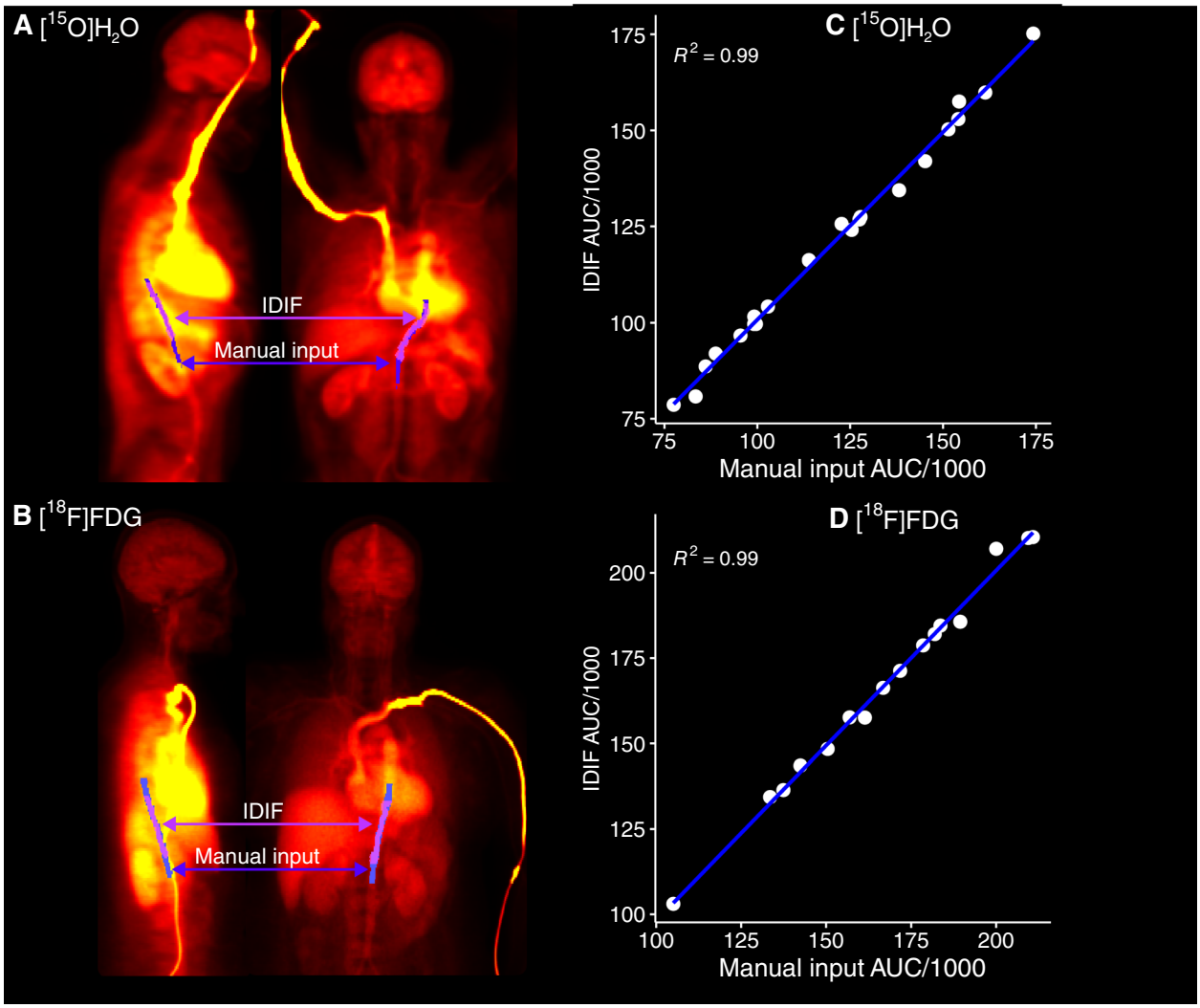


**Fig. 2** **A-B)** Manually delineated descending aorta ROI (blue) overlaid with image-derived input (violet) for $[^{15}O]H_2O$ and for $[^{18}F]FDG$. **C-D)** Scatterplots of areas under the input curves of manually delineated descending aorta and image-derived input for $[^{15}O]H_2O$ and for $[^{18}F]FDG$.

identify the starting point. From this level, the maximums are located from each axial slice and connected transaxially by gap-filling algorithm 10 cm downwards to form a continuous, string-like ROI along the aorta. (Fig. 2A-B).

### Brain-PET data analysis

The brain consists of distinct cytoarchitectonical and functionally separable regions, which are previously defined in various atlases in standard stereotactic space. Therefore, a separate analysis pathway is used to incorporate these atlases and to facilitate whole-brain analysis using widely used toolboxes (e.g., SPM, FSL) based on parametric mapping of spatially normalized brain images. In this stream, a freely available in-house Magia-toolbox [2] is used for extracting the brain from the original PET image, followed by rigid motion correction and spatial radioligand template-based normalization for transforming the desired atlas from standard Montreal Neurological Institute (MNI) space to the subject native space. The pipeline includes the ROIs from AAL-atlas [19] containing cortical lobes and selected subcortical regions, but any other atlas in MNI space can also be used by including the binary brain ROI NIfTI-files in the corresponding ROI folder. Finally, kinetic modelling is carried out for each region, as well as at the voxel-level for the whole brain data.

### Output

As a result, the parameter estimates, CT-based ROI volumes, and model goodness of fit metric (Pearson's $R^2$ used as a descriptive measure of correspondence between observed TACs and model-predicted values) are saved for each region in the standard format. These results can then

be retrieved for selected subjects using a dedicated function. Regional results from voxel-level parameter maps and from clustered regions can also be collected similarly. The voxel-level parameter maps are also clustered into three subregions within selected areas using hierarchical clustering. This supports regional analysis of functionally distinct areas, such as the kidney cortex and medulla or brain grey and white matter. Additionally, quality control plots illustrating the CT to PET registration, corrected PET motion, regional model fits and overlay-images of CT and voxel-level parameters are saved in an html-file for later visual check (see **Online Resource** for example of quality control output).

## Validation

We validated the automated [$^{15}$O]$H_2O$ and [$^{18}$F]FDG analysis pipeline by 1. comparing automatically and manually derived input functions, 2. assessing the agreement between regional and voxel-level modelling, 3. evaluating the effect of motion correction, and 4. comparing the results from manual and automatic ROI delineation.

For validation purposes in the main report, we chose six segmented CT-based ROIs (cortical brain grey matter (GMctx), left iliopsoas muscle, right kidney cortex and medulla, pancreas, spleen and liver) representing different levels of perfusion and glucose metabolism. The results from all other segmented regions (n = 72; ribs and vertebrae are excluded for clarity), are shown in the **Online Resource**. To account for the contribution of arterial blood, perfusion was quantified as $H_2O_{flow} = K_1(1\text{-}V_A)$, and glucose metabolism was quantified as Patlak $K_i$. Because the dual input [$^{15}$O]$H_2O$ model in the liver may have parameter identifiability issues in $K_1$ and $k_2$ parameters, we repeated the liver analysis using distribution volume $K_1/k_2$ (see **Online Resource**).

The accuracy of the automatically derived descending aorta IDIF was tested by comparing the model parameter estimates from segmented CT-based ROIs using both automated and manually drawn input, which was delineated using the above-described criteria with Carimas software [20]. Agreement between regional and voxel-level estimates was evaluated by comparing parameters estimated from averaged regional TACs to voxel-level estimates averaged within each ROI. To evaluate the effect of motion correction, parameter estimates from motion-corrected and uncorrected data were compared using CT-based ROIs.

To assess ROI delineation, modelling results based on the descending aorta IDIF were compared between manually drawn and automatically segmented CT-based ROIs. For [$^{15}$O]$H_2O$, two axial ROIs (liver, kidney cortices) and an ellipsoid-shaped spleen ROI were drawn by one observer, while for [$^{18}$F]FDG, two axial ROIs (iliopsoas muscle, liver) were drawn independently by two observers. Because the manually drawn ROIs were substantially smaller than the automatically segmented ones, voxel-level results from manual ROIs in the liver and spleen were also compared with results from CT-based ROIs where the volume was reduced using image erosion in MATLAB (20 mm from the ROI borders in the liver and 10 mm in the spleen; these distances were chosen mainly to mitigate the effect of heart and respiratory motion, and the user can modify these margins freely for any segmented organ within TurBO). Similar comparisons using voxel level results were performed between manual ROIs and PET-based clusters in the kidney cortex, as well as between PET-based cortical GMctx clusters and results of the corresponding AAL-atlas ROI from the PET-template-based brain processing. Finally, for [$^{15}$O]$H_2O$, we also compared myocardial blood flow (MBF) measured as $k_2$ with descending aorta IDIF to manually assessed MBF using Carimas software with left ventricle input [21].

All regional [$^{15}$O]$H_2O$ parameter estimates were calculated using non-linear least squares (NNLS) estimation with 100 randomly initialized parameters from the following lower and upper bounds: $K_1$:[0, 1800] ml/(min*dl), $K_1/k_2$:[0, 1], $V_A$:[0, 0.8]. Voxel-level [$^{15}$O]$H_2O$ parameters were estimated using the pipeline default values – 500 basis functions with uniformly distributed $k_2$ values from the range [0, 6] 1/min.

## Validation data

The automated processing and kinetic modelling for perfusion imaging was validated using LAFOV [$^{15}$O]$H_2O$ PET data from 21 healthy subjects, which were acquired at Turku PET centre with Biograph Vision Quadra (Siemens Healthineers) PET/CT scanner with spatial resolution of 3.3–3.8 mm FWHM and an axial field of view of 106 cm [22]. Validation for imaging the glucose metabolism was carried out using the same scanner with [$^{18}$F]FDG PET data from healthy control and obese subjects (n = 16). Data acquisition and subject's demographic details are described in the **Online Resource**. The study was approved by the institutional ethical review board and conducted following the principles of the Declaration of Helsinki. All participants provided written informed consent prior to the examinations.

## Statistical methods

All statistical comparisons were carried out in R (version 4.4.1) using Pearson's correlation and Bland–Altman analysis describing the relative difference and 95% limits of agreement between the methods. Paired t-test was used to assess the significant differences between the methods, where $p < 0.05$ indicated a statistical significance.

## Results

### Processing time

The mean (SD) processing time per subject was 91.0 (7.5) minutes for [$^{15}$O]$H_2O$ data, and 80.8 (3.6) minutes for [$^{18}$F]FDG data, using computational server equipped with an Intel® Xeon® Platinum 8468V processor (97.5 MB cache, 2.40 GHz, 96 cores), 900 GB RAM, and an NVIDIA L40 GPU (46 GB VRAM). Processing was performed with 25 parallel MATLAB workers on MATLAB R2024a running under Ubuntu Linux (version 22.04.5 LTS) (Online Resource, Table S2).

### Model fits

Visual inspection indicated high quality model fits in all regions, except in kidneys, where the model underestimated the measured TAC in the later time points. There was a moderate variability between subjects, but data and model fits had a high correlation across subjects (mean $R^2>0.88$ for [$^{15}$O]$H_2O$, and mean $R^2>0.92$ for [$^{18}$F]FDG) in all studied regions (Fig. 3).

### Automated versus manual ROI delineation

There was moderate overlap between the manually drawn and automatically derived input function mask images for both datasets, and in the [$^{18}$F]FDG data the manual input volume was larger than the IDIF volume (Online Resource, Table S3). Despite this, the areas under the curves (AUCs) of manually derived input function and IDIF (Fig. 2C-D) were almost perfectly correlated ($R^2=0.99$).

The parameter estimates using manual and automatically derived input functions had high correlation ($R^2>0.74$ for [$^{15}$O]$H_2O$, and $R^2>0.78$ for [$^{18}$F]FDG) in all selected six regions, with negligible bias for both radioligands (Fig. 4:manual vs. automatic input, Online Resource, Figure S4). When all regions were considered, the correlation and bias results were similar, but lower correlation and higher mean relative difference were observed in arteries and in heart and lung subregions mainly for [$^{15}$O]$H_2O$ (Online Resource, Figure S5).

### Motion correction

To estimate the regional motion for each subject, we tracked the Euclidean distance of a single voxel, located at the mean of x-, and the maximum of y-, and z-coordinates in each segmented ROI, between the data with and without motion correction, and the results of corrected frame-wise motion for each ROI are summarized in Online Resource, Table S4. Despite of the motion, parameter estimates using motion-corrected data were associated ($R^2>0.71$ for [$^{15}$O]$H_2O$, and $R^2>0.78$ for [$^{18}$F]FDG) with the estimates obtained using uncorrected data (Fig. 4:uncorrected vs. motion corrected). The mean relative difference varied by region, with higher difference in the right kidney (24%) and in pancreas (13%) in [$^{15}$O]$H_2O$ data and in the right kidney (−27%) and in spleen (−11%) in [$^{18}$F]FDG data, compared to the other selected regions. When all regions were considered, lower correlation and higher mean relative difference were found mainly in arteries and in the heart (Online Resource, Figure S6).

### Regional versus voxel-level results

Despite significant differences in brain for both [$^{15}$O]$H_2O$ and [$^{18}$F]FDG, and in pancreas and spleen for [$^{15}$O]$H_2O$, the regional and voxel-level modelling results were highly correlated ($R^2>0.83$ for [$^{15}$O]$H_2O$, and $R^2>0.99$ for [$^{18}$F]FDG) for both radioligands (Fig. 4:ROI vs. VOX,Fig. 5). The mean relative difference between regional and voxel-level [$^{18}$F]FDG modelling was less than 2%, and below 10% for [$^{15}$O]$H_2O$. When all regions were considered, lower correlation and higher mean relative difference were observed only in [$^{15}$O]$H_2O$ data in arteries, lungs and in heart (Online Resource, Figure S7).

Voxel-level results obtained using the basis function method yielded higher correlation, and less bias with the ROI-level modelling results compared to the results of the voxel-level model, where all three parameters were estimated (Online Resource, Figure S8). Liver distribution volumes ($K_1/k_2$) showed similar results in all validation tests 1–3, as compared with the $H_2O_{flow}$ ($K_1(1-V_A)$) estimates (Online Resource, Figure S9), but with a significantly lower coefficient of variation (6.8% in $K_1/k_2$ vs. 65.8% in $H_2O_{flow}$ estimates).

Manually drawn ROIs were substantially smaller than the automatically segmented CT-based ROIs (Online Resource, Table S5). However, comparison between [$^{15}$O]$H_2O$ and [$^{18}$F]FDG parameter estimates from manually delineated ROIs and segmented CT ROIs showed high correlation ($R^2>0.82$ for [$^{15}$O]$H_2O$, and $R^2>0.83$ for [$^{18}$F]FDG), but moderate mean relative differences (18% in kidney, 21% in spleen, 10% in liver and 8% in myocardium for [$^{15}$O]$H_2O$, and −19% in liver and 7% in iliopsoas muscle for [$^{18}$F]FDG; Fig. 6).

After reducing the volumes of segmented liver and spleen CT ROIs, the voxel level parameter estimates were more closely aligned with the results from manually drawn ROIs in the liver for [$^{15}$O]$H_2O$, but there were significant differences in the spleen for [$^{15}$O]$H_2O$ and in liver for [$^{18}$F]FDG based on paired t-test (Fig. 7). Similarly, PET-based clustering gave corresponding estimates in the brain as compared to the results of PET-template based processing, but in the kidney, the clustered cortex ROI produced significantly higher estimates compared to the manually drawn cortex ROI for [$^{15}$O]$H_2O$ (Fig. 7).

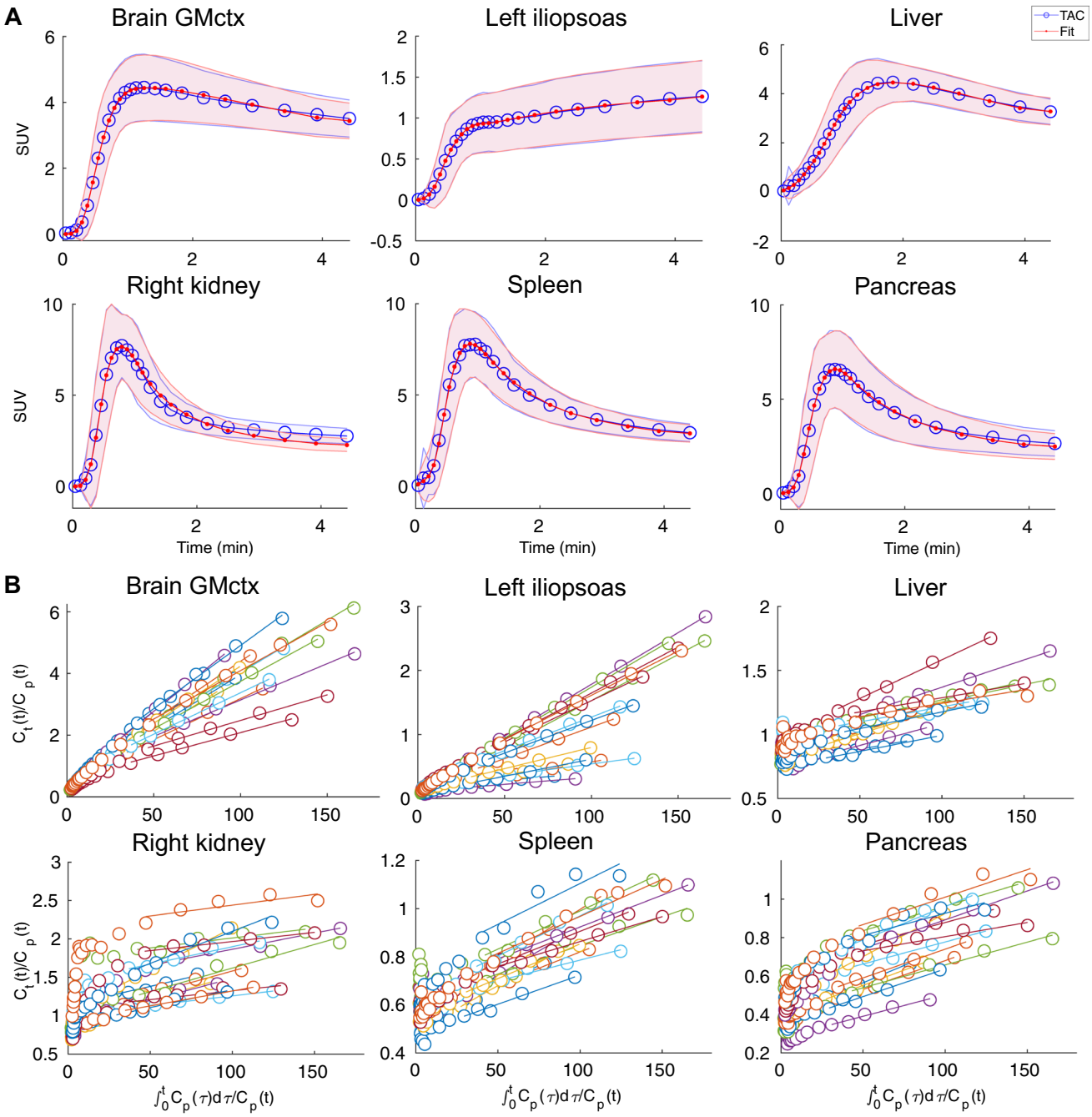


**Fig. 3** **A)** Between subject mean [$^{15}$O]$H_2O$ PET time-activity curves (blue) and the mean one tissue compartment model fits (red) in brain cortical grey matter (GMctx), left iliopsoas muscle, liver, right kidney, spleen and pancreas for 21 subjects scanned at rest. Shaded areas illustrate the standard deviation of the data and the corresponding model fits. **B)** [.$^{18}$F]FDG Patlak-plots in GMctx, left iliopsoas muscle, liver, right kidney, spleen and pancreas for 16 subjects (shown in different colours)

## Discussion

We developed a unified pipeline for LAFOV PET data processing and kinetic modelling and demonstrated that it produces consistent regional estimates of radiotracer uptake for both tested radioligands [$^{15}$O]$H_2O$ and [$^{18}$F]FDG. In contrast with existing pipelines that are limited to specific tissues such as the brain [2, 4, 5] or can handle only a single step of the data preprocessing such as kinetic modelling [23, 24], the TurBO pipeline provides a complete workflow tailored for whole-body LAFOV PET. It integrates image registration, segmentation, motion correction, and both region- and voxel-level kinetic modelling within a single comprehensive framework, offering broader functionality than previously

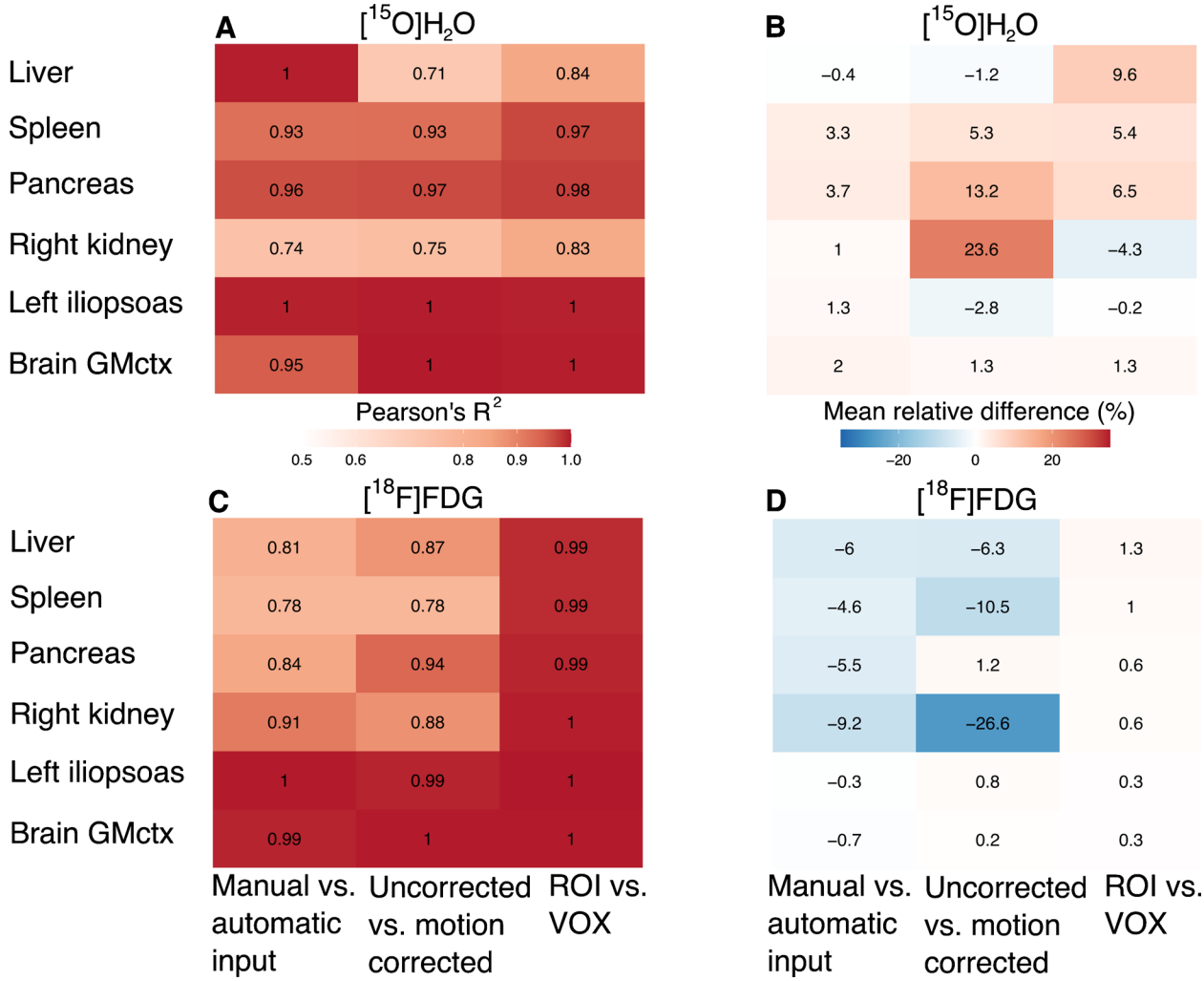


**Fig. 4** Comparisons between manual vs. automatic input determination methods, motion corrected and uncorrected data, and regional-level versus voxel-level (ROI vs. VOX) methods**. A)** Correlation coefficients (Pearson's $R^2$) and **B)** mean relative regional differences (%) of regional $[^{15}O]H_2O$ parameter estimates. **C)** Correlation coefficients (Pearson's $R^2$) and **D)** mean relative regional differences (%) of regional $[^{18}F]$FDG Patlak $K_i$

available packages. By automating all processing stages and systematically logging parameters, TurBO improves reproducibility and reduces inter-operator variability in ROI delineation. Overall, this approach allows standardized large-scale analysis of LAFOV PET data, paving the way for harmonized analysis and data integration in multi-centre studies.

## Robust automated input delineation and modelling in regional and voxel-level

PET data kinetic modelling requires the input function typically obtained either from blood samples or from the image. Blood sampling introduces additional labour to the imaging protocol, but with sufficiently long axial FOV and short imaging frames, the input can be derived reliably from the aorta if it is visible in the image [25]. Our results confirm that the automatic input delineation implemented in the TurBO pipeline is robust and comparable with manual delineation, and thus it can be reliably used instead of time-consuming manual input ROI drawing.

We also established that the regional outcome measures had high correlation between manually and automatically derived ROIs, and between voxel-level and region-level analyses. Voxel-level $[^{15}O]H_2O$ modelling with basis functions improved alignment with the ROI-based results, when compared to the full three-parameter voxel-level model. However, this method requires more processing time because the delay parameter must be estimated for each voxel. Nevertheless, all processing and modelling for one subject was completed in 91 min for our $[^{15}O]H_2O$ and 81 min for our $[^{18}F]$FDG data. With parallel computing, larger batches can be completed in a day, depending on the available resources.

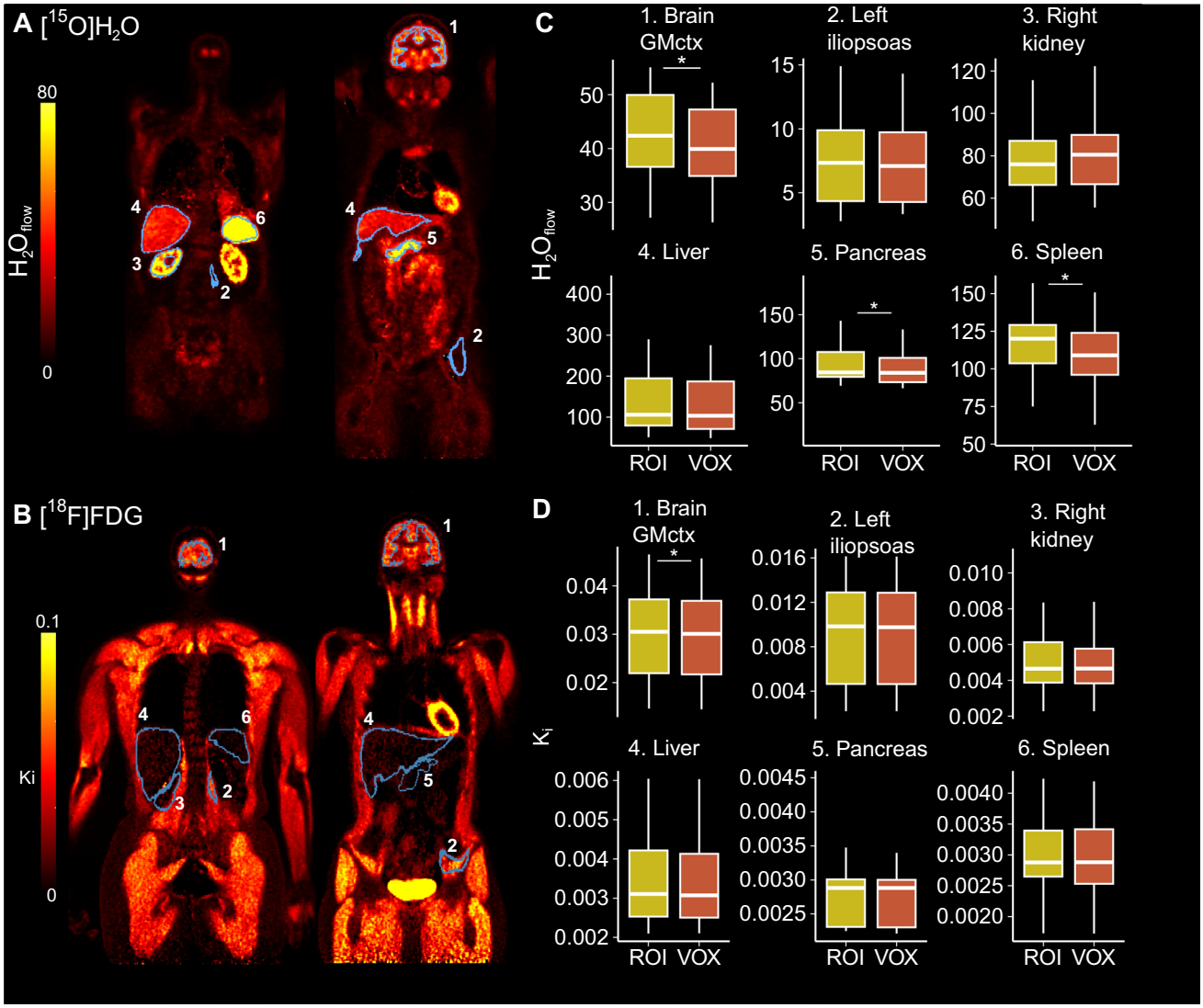


**Fig. 5** Voxel-level average intensity projection images for representative subjects: **A)** $H_2O_{flow}$ image for [$^{15}$O]$H_2O$ and **B)** $K_i$ image for [$^{18}$F]FDG. **C-D)** Boxplots illustrating the regional (ROI) and voxel-level (VOX) estimates in brain cortical grey matter (GMctx), left iliopsoas muscle, right kidney, pancreas and spleen for [$^{15}$O]$H_2O$ (n = 21) and [$^{18}$F]FDG (n = 16) data. Significant differences based on paired t-test are indicated with asterisks

Altogether, these results show, that TurBO provides a reproducible, reliable and computationally fast approach for modelling and investigating LAFOV PET data and facilitates the investigation of inter-organ interactions in tissue perfusion and metabolism.

## Motion correction

While controlling subject motion is crucial for obtaining high-quality data, involuntary movements, such as breathing and cardiac motion are still present during image acquisition, as observed in our motion correction results. Although the motion during PET scanning and misalignment between CT and PET should ideally be corrected during image reconstruction, our pipeline also includes post-reconstruction correction methods. To account for complex body movements, we included in our pipeline a diffeomorphic correction method [7], that employs both rigid and nonlinear deformations. Our findings showed a high correlation between corrected and uncorrected data, but noticeable differences in absolute values, especially in the kidney and pancreas, which highlights the importance of motion correction.

Although previous research suggests that cardiac motion may require nonlinear correction methods [26], the recent findings have showed that rigid correction methods may be sufficient [27]. For practical reasons, we applied only rigid motion correction when deriving the IDIF. This approach minimizes alterations to the original data and avoids potential

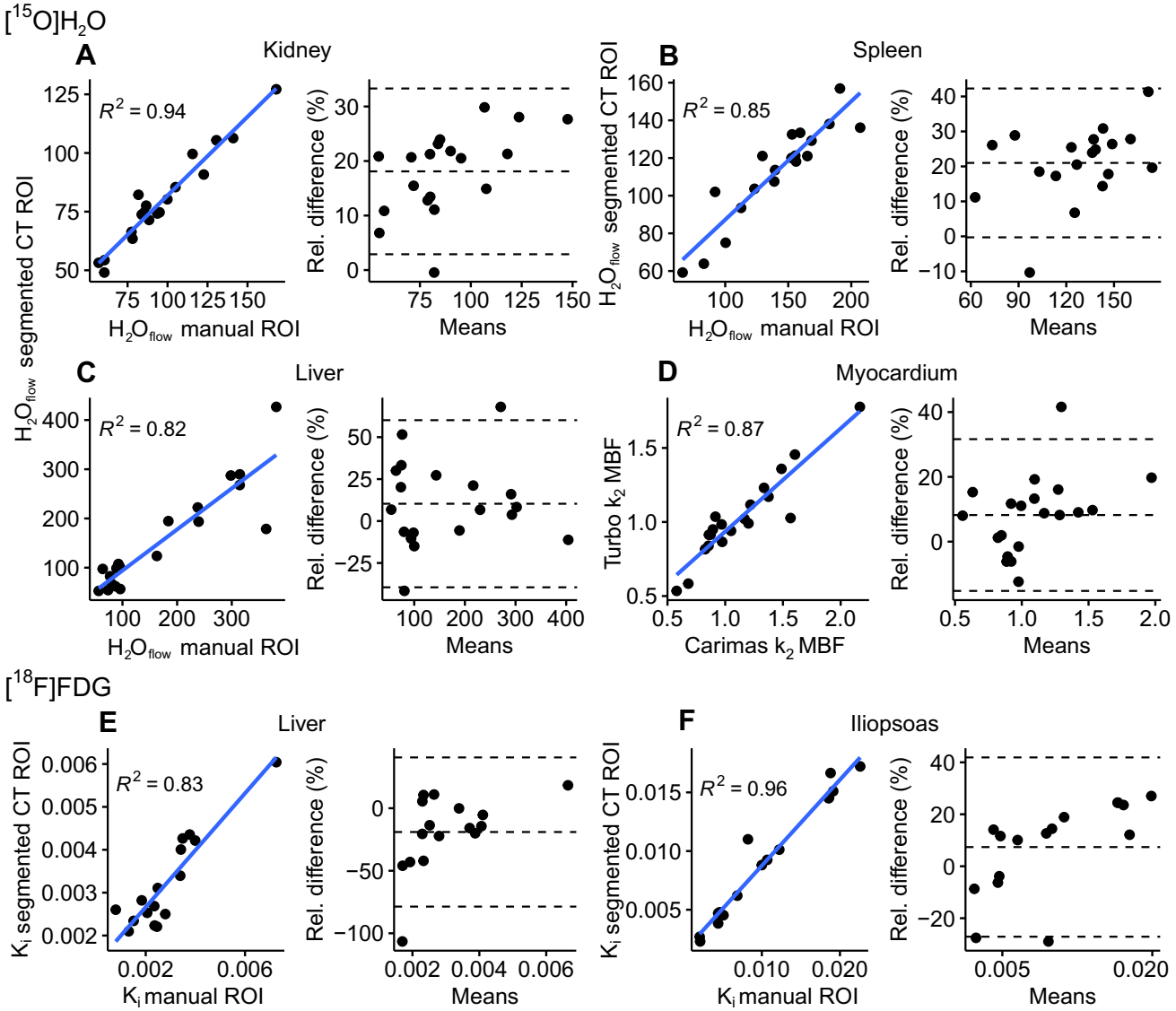


**Fig. 6 A-C)** Scatterplots and Bland–Altman plots illustrating the correlation and relative difference between $[^{15}O]H_2O$ parameter estimates of interest in manually drawn ROIs and segmented CT-based ROIs. **D)** Scatterplot and Bland–Altman plot illustrating the correlation and relative difference between myocardial blood flow (MBF) measured as $k_2$ with descending aorta IDIF and manually assessed $k_2$ MBF with left ventricle input. **E–F)** Scatterplots and Bland–Altman plots illustrating the correlation and relative difference between $[^{18}F]$FDG Patlak $K_i$ in manually drawn ROIs and segmented CT ROIs

image distortions that could arise from diffeomorphic correction. Additionally, the method allows for correcting also the initial frames, which is not feasible in the diffeomorphic LAFOV motion correction [7]. Based on our results the automated IDIF produced comparable results with the manually derived input without motion correction. The remaining small bias between the results of the automated and manual methods is likely caused by differences in the input ROI volumes, and because the subject motion is corrected in the automated IDIF.

## Impact of ROI delineation methods

Apart from the input, the other manually drawn ROIs were substantially smaller than the automatically segmented CT-based ROIs, because the manual ROIs were drawn only to a limited number of slices. This likely explains the relative differences between the regional results from automatically derived and manual ROIs, as well as the high variability in the high-flow regions such as the kidneys, and pancreas which are also prone to the cardiac and respiratory motion.

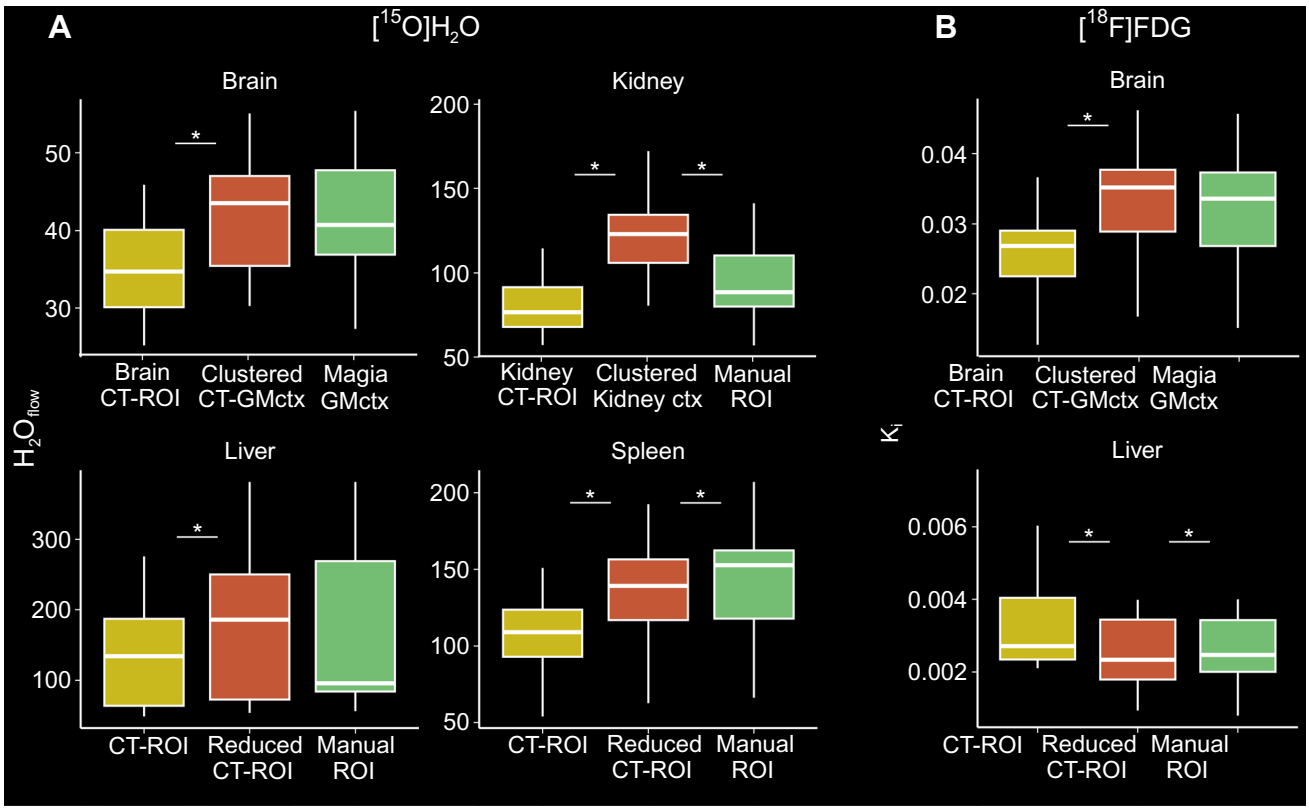


**Fig. 7** Boxplots illustrating **A)** [$^{15}$O]$H_2O$ (n = 21) and **B)** [$^{18}$F]FDG (n = 16) voxel-level results using manually drawn ROIs, CT-based ROIs, CT-based ROIs where the volume was reduced (in liver and spleen), and PET-based clustered ROIs (in brain and kidneys). Significant differences based on paired t-test with respect to clustered- and reduced ROIs are indicated with asterisks

Because the CT-based segmented ROIs are large entities, the pipeline includes also additional reduced ROIs, which mitigate the effects of subject motion and spill in from other nearby regions. Also, hierarchical clustering of voxel-based parametric maps within a selected region into separate subregions allow to examine the functionally distinct subregions, such as the kidney cortex and medulla.

## Limitations

Although the CT segmentation is generally robust and the current quality control reports segmented ROI volume statistics, visual inspection of the ROIs is recommended to ensure correct segmentation and to identify potential anomalies, or other confounding factors. The radiowater model in the liver may have issues with parameter identifiability due to the dual input model [28]. Although the validation results were similar between $H_2O_{flow}$ ($K_1(1-V_A)$) and distribution volume $K_1/k_2$, the coefficient of variation was significantly lower for $K_1/k_2$ and thus, it would be the preferred measure for quantification, but as the model and the dual input may still require further validation, the results should be interpreted with caution. There was also a discrepancy between the region-level and voxel-level results in [$^{15}$O]$H_2O$ data in arteries, lungs, and the heart, which likely occurs due to high arterial volume fraction in these regions. Particularly, the $K_1$ and $V_A$ parameters of 1TCM are highly correlated in regions with high arterial volume fraction and cannot be reliably estimated. In such regions, it is possible to used fixed value ($V_A$) for arterial volume fraction, which may help to overcome the parameter identifiability issues.

Model fits were generally satisfactory across regions, except in the kidneys in [$^{15}$O]$H_2O$ data, where slight underestimation was observed in the later time points, likely due to complex tracer kinetics behaviour that is not well described by the standard [$^{15}$O]$H_2O$ 1TCM. Since this deviation occurs only in the later part of the scan, perfusion may still be reliably estimated using the earlier data, although the current results should be interpreted with caution. However, the pipeline is flexible and modular and tailored models with customized inputs can be included, but this warrants further research and careful validation.

## Future directions

Potential improvements may include pseudo-CT segmentation to reduce possible misalignment between CT and PET images, even though our pipeline already co-registers CT to the PET mean image. This might be useful especially in multi-scan studies where acquiring additional reference CT images would increase the radiation load significantly. Another future direction is the spatial normalization of LAFOV data to a standard template, which is a common approach in brain imaging. Creating such LAFOV templates for specific tracers would enable voxel-level statistical analysis, which would expand the restricted local regional analysis further to cover the full total-body image volume. Finally, due to the modular structure, the TURBO pipeline can be extended with additional kinetic models to allow its use to other tracers beyond $[^{15}O]H_2O$ and $[^{18}F]FDG$.

## Conclusion

TurBO pipeline provides a reproducible, reliable and computationally fast approach for analysing LAFOV PET data and enables interorgan interaction studies in tissue perfusion and metabolism.

**Supplementary Information** The online version contains supplementary material available at https://doi.org/10.1007/s00259-026-07769-7.

**Acknowledgements** This study was supported by European Research Council (ERC-ADV #101141656), Jane and Aatos Erkko Foundation and Gyllenberg's Stiftelse, the Finnish Foundation for Cardiovascular Research, Finnish State Research Funding (VTR), Finnish Cultural Foundation, InFLAMES research flagship, Gyllenberg's Stiftelse and Research Council of Finland (formerly Academy of Finland) academy research fellowship grant #360120. The authors thank all study participants and the staff at the Turku PET Centre for their assistance.

**Author contributions** The authors have contributed as follows: LN, PN and JK supervised the study; HK, ALR, NT and HH performed the subject recruitment and PET scanning; JT and SP implemented the pipeline, processed the data and evaluated the results; VO, HI, TK, RK, SP and JT supervised the kinetic modelling and implemented the methods; CH performed the manual cardiac analysis; AKK and JR performed the radiochemistry; JaT contributed to the data reconstruction and pipeline evaluation; SVN, HK, ALR, NT carried out the manual ROI drawing; JT, SP and LN drafted the manuscript; All authors interpreted the results, critically revised the article, and approved of the final version for publication.

**Funding** Open Access funding provided by University of Turku (including Turku University Central Hospital). This work was supported by the European Research Council (Advanced Grant #101141656 to Lauri Nummenmaa), Jane and Aatos Erkko Foundation, the Finnish Foundation for Cardiovascular Research, Finnish State Research Funding (VTR), Finnish Cultural Foundation, InFLAMES research flagship, Gyllenberg's Stiftelse and Research Council of Finland (formerly Academy of Finland) academy research fellowship grant #360120 to Jarmo Teuho).

**Data availability** According to the local ethics committee, sharing even anonymized medical imaging data is not permitted. TurBO pipeline code is freely available at https://turbo.utu.fi/.

## Declarations

**Ethical approval** The study was approved by the institutional ethical review board and conducted following the principles of the Declaration of Helsinki.

**Consent to participate** Informed consent was obtained from all individual participants included in the study.

**Consent to publish** The authors affirm that human research participants provided informed consent for publication of the images in Figs. 1, 2a, 2b, 5a and 5b.

**Competing interests** Dr. Knuuti received consultancy fees from GE Healthcare and Synektik and speaker fees from Siemens Healthineers, outside of the submitted work.



## References

1. Knuuti J, Tuisku J, Kärpijoki H, Iida H, Maaniitty T, Latva-Rasku A, et al. Quantitative perfusion imaging with total-body PET. J Nucl Med J Nucl Med. 2023;64:11S-19S.
2. Karjalainen T, Tuisku J, Santavirta S, Kantonen T, Bucci M, Tuominen L, et al. Magia: robust automated image processing and kinetic modeling toolbox for PET Neuroinformatics. Front Neuroinf. 2020;14:3.
3. Greve DN, Svarer C, Fisher PM, Feng L, Hansen AE, Baare W, et al. Cortical surface-based analysis reduces bias and variance in kinetic modeling of brain PET data. Neuroimage Neuroimage. 2014;92:225–36.
4. Gunn R, Coello C, Searle G. Molecular imaging and kinetic analysis toolbox (MIAKAT)-a quantitative software package for the analysis of PET neuroimaging data. J Nucl Med. 2016;57:1928.
5. Funck T, Larcher K, Toussaint PJ, Evans AC, Thiel A, Frontiers Media S.A. APPIAN: Automated pipeline for PET image analysis. Front Neuroinform. 2018;12:408902.
6. Li X, Morgan PS, Ashburner J, Smith J, Rorden C. The first step for neuroimaging data analysis: DICOM to NIfTI conversion. J Neurosci Methods. 2016;264:47–56.
7. Sundar LKS, Lassen ML, Gutschmayer S, Ferrara D, Calabrò A, Yu J, et al. Fully automated, fast motion correction of dynamic whole-body and total-body PET/CT imaging studies. J Nucl Med. 2023. https://doi.org/10.2967/jnumed.122.265362.
8. Wasserthal J, Breit HC, Meyer MT, Pradella M, Hinck D, Sauter AW, et al. TotalSegmentator: robust segmentation of 104 anatomic

structures in CT images. Radiol Artif Intell. 2023;5(5):e230024. https://doi.org/10.1148/ryai.230024.
9. Kety SS, Schmidt CF, American Society for Clinical Investigation. The nitrous oxide method for the quantitative determination of cerebral blood flow in man: theory, procedure and normal values. J Clin Invest. 1948;27:476.
10. Ziegler SI, Haberkorn U, Byrne H, Tong C, Schosser R, Krieter H, et al. Measurement of liver blood flow using oxygen-15 labelled water and dynamic positron emission tomography: limitations of model description. Eur J Nucl Med. 1996;23:169–77.
11. Kudomi N, Slimani L, Järvisalo MJ, Kiss J, Lautamäki R, Naum GA, et al. Non-invasive estimation of hepatic blood perfusion from H2 15O PET images using tissue-derived arterial and portal input functions. Eur J Nucl Med Mol Imaging. 2008;35:1899–911.
12. Lawson CL, Hanson RJ. Solving least squares problems. Society for Industrial and Applied Mathematics; 1995.
13. Kudomi N, Koivuviita N, Liukko KE, Oikonen VJ, Tolvanen T, Iida H, et al. Parametric renal blood flow imaging using [15O] H2O and PET. Eur J Nucl Med Mol Imaging. 2009;36:683–91.
14. Phelps ME, Huang SC, Hoffman EJ, Selin C, Sokoloff L, Kuhl DE. Tomographic measurement of local cerebral glucose metabolic rate in humans with (F-18)2-fluoro-2-deoxy-D-glucose: validation of method. Ann Neurol. 1979;6:371–88.
15. Patlak CS, Blasberg RG, Fenstermacher JD. Graphical evaluation of blood-to-brain transfer constants from multiple-time uptake data. J Cereb Blood Flow Metab. 1983;3:1–7.
16. Rutland M, Que L, Hassan IM. 'FUR'–one size suits all. Eur J Nucl Med. 2000;27:1708–13.
17. Dias AH, Hansen AK, Munk OL, Gormsen LC, Springer Science and Business Media Deutschland GmbH. Normal values for 18F-FDG uptake in organs and tissues measured by dynamic whole body multi-parametric FDG PET in 126 patients. EJNMMI Res. 2022;12:15.
18. Nordstrom J, Kero T, Lindstrom E, Sigfridsson J, Sorensen J, Lubberink M. 2024 Cardiac 15O-water PET motion correction using patient specific synthetic dynamic images. Eur Hear J - Cardiovasc Imaging. Oxford Academic; 25.
19. Tzourio-Mazoyer N, Landeau B, Papathanassiou D, Crivello F, Etard O, Delcroix N, et al. Automated anatomical labeling of activations in SPM using a macroscopic anatomical parcellation of the MNI MRI single-subject brain. Neuroimage. 2002;15:273–89.
20. Rainio O, Han C, Teuho J, Nesterov SV, Oikonen V, Piirola S, et al. Carimas: an extensive medical imaging data processing tool for research. J Digit Imaging. 2023;36(4):1885–93.
21. Nesterov SV, Han C, Mäki M, Kajander S, Naum AG, Helenius H, et al. Myocardial perfusion quantitation with 15O-labelled water PET: High reproducibility of the new cardiac analysis software (Carimas$^{TM}$). Eur J Nucl Med Mol Imaging. 2009;36:1594–602.
22. Prenosil GA, Sari H, Fürstner M, Afshar-Oromieh A, Shi K, Rominger A, et al. Performance Characteristics of the Biograph Vision Quadra PET/CT System with a Long Axial Field of View Using the NEMA NU 2–2018 Standard. J Nucl Med. 2022;63:476–84.
23. Besson FL, Faure S. PET kinetix-a software solution for PET parametric imaging at the whole field of view level. J Imaging Inform Med. 2024;37:842–50.
24. Tjerkaski J, Cervenka S, Farde L, Matheson GJ. Kinfitr — an open-source tool for reproducible PET modelling: validation and evaluation of test-retest reliability. EJNMMI Res. 2020;10(1):77.
25. Palard-Novello X, Visser D, Tolboom N, Smith CLC, Zwezerijnen G, van de Giessen E, et al. Validation of image-derived input function using a long axial field of view PET/CT scanner for two different tracers. EJNMMI Phys. 2024;11:1–13.
26. Lamare F, Le Maitre A, Dawood M, Schäfers KP, Fernandez P, Rimoldi OE, et al. Evaluation of respiratory and cardiac motion correction schemes in dual gated PET/CT cardiac imaging. Med Phys. 2014;41:072504.
27. Christensen NL, Nordström J, Madsen S, Madsen MA, Gormsen LC, Kero T, et al. Detection and correction of patient motion in dynamic $^{15}$O-water PET MPI. J Nucl Cardiol. 2023;30:2736–49.
28. Becker GA, Müller-Schauenburg W, Spilker ME, Machulla HJ, Piert M, IOP Publishing. A priori identifiability of a one-compartment model with two input functions for liver blood flow measurements. Phys Med Biol. 2005;50:1393.